

Dynamical correlations and chimera-like states of nanoemitters coupled to plasmon-polaritons in a lattice of conducting nanorings

Boris A. Malomed^{1,2}, Gennadiy Burlak^{*3}, Gustavo Medina-Ángel^{3,4}, and Yuriy Karlovich⁵ 1, 2, 3, 4, 5, a)

¹⁾*Department of Physical Electronics, School of Electrical Engineering, Faculty of Engineering, and Center for Light-Matter Interaction, Tel Aviv University, P.O.B. 39040, Tel Aviv, Israel*

²⁾*Instituto de Alta Investigación, Universidad de Tarapacá, Casilla 7D, Arica, Chile*

³⁾*CIICAp, Universidad Autónoma del Estado de Morelos, Av. Universidad 1001, Cuernavaca, Morelos 62209, México*

⁴⁾*FCAeI, Universidad Autónoma del Estado de Morelos, Av. Universidad 1001, Cuernavaca, Morelos 62209, México*

⁵⁾*CInC, Universidad Autónoma del Estado de Morelos, Av. Universidad 1001, Cuernavaca, Morelos 62209, México*

We systematically investigate semiclassical dynamics of the optical field produced by quantum nanoemitters (NEs) embedded in a periodic lattice of conducting nanorings (NRs), in which plasmon polaritons (PPs) are excited. The coupling between PPs and NEs through the radiated optical field leads to establishment of a significant cross-correlation between NEs, so that their internal dynamics (photocurrent affected by the laser irradiation) depends on the NR's plasma frequency ω_p . The transition to this regime, combined with the nonlinearity of the system, leads to a steep increase of the photocurrent in the NEs, as well as to non-smooth (chimera-like or chaotic) behavior in the critical (transition) region, where small variations of ω_p lead to significant changes in the level of the NE pairwise cross-correlations. The chimera-like state is realized as coexistence of locally synchronized and desynchronized NE dynamical states. A fit of the dependence of the critical current on ω_p is found, being in agreement with results of numerical simulations. The critical effect may help to design new optical devices, using dispersive nanolattices which are made available by modern nanoelectronics.

^{a)}Electronic mail: gburlak@uaem.mx, malomed@tauex.tau.ac.il, gustavo.isc@hotmail.com, karlovich@uaem.mx

I. INTRODUCTION

The current work in the field of infrared photoelectric information technologies yields advances in the generation, manipulations, source detection, and related achievements in the field of infrared photonics¹⁻⁶. The inclusion of dispersive nanorings (NRs) in the operation of nanoemitters (NEs) considerably affects the generated electromagnetic field, whose structure significantly depends on the NR's plasma frequency, ω_p ^{7,8}. In such hybrid systems, it is possible to control properties of local optical fields and the creation of miniaturized low-threshold coherent tunable sources^{8,9}. An essential feature of these structures in the disordered state is that NE clusters produce fractal radiation patterns, in which light is simultaneously emitted and scattered¹⁰. In the practically relevant case of lossy NRs with embedded NEs, other factors become important too. Optical fields of dispersive NRs perturb the energy levels of NEs, hence plasmon polaritons (PPs) populating NRs affect the internal degrees of freedom of the quantum NEs coupled to the NRs. Nonlinearity is an important feature of NEs, which leads to laser emission¹¹. All that leads to resonant changes in the field structure associated with the PP excitation in the NRs. We found that such a system exhibits coexistence of locally synchronized and desynchronized dynamics of random NEs, which may be considered as a chimera-like behavior in the respective range of ω_p . We remind that a “chimera state” is a dynamical pattern that occurs in a network of coupled identical oscillators when the oscillator population is broken into synchronous and asynchronous parts¹². The PP field being external to the field in the NEs, at small values of ω_p the NE dynamics is practically independent of ω_p . However, at overcritical values of ω_p , i.e., above the transition to the state with the strong coupling of the NR and NE subsystems, the NE photocurrent essentially depends on ω_p .

In this paper we theoretically study dynamics and correlations of quantum NEs embedded in a periodic lattice of conducting NRs, in which the PPs are excited. We show that the coupling between PPs and NEs through the optical field leads to a significant correlation between NEs, so that the internal dynamics of the NEs (quantum photocurrent) depends on the plasma frequency ω_p of the classical subsystem of PPs in the NR. Thus, the setup is built of two subsystems coupled by the radiation field, *viz.*, the classical array of the NRs and the quantum (actually, semi-classical) subsystem of NEs. We consider conducting (carbon) NRs, whose properties are determined by ω_p . The PP field interacts with NEs and perturbs

its quantum degrees of freedom. We show that the field dynamics is distinct in different ranges of ω_p , which can be separated by some characteristic value ω_c . At small $\omega_p < \omega_c$, the PP field has a small amplitude, weakly perturbing the quantum dynamics and securing smooth cross-correlations of the NEs. However, at larger $\omega_p \geq \omega_c$, a transition occurs to the state in which the PP field produces a significant contribution to the radiation, which perturbs the dynamics of NEs, leading to a change in their cross-correlations.

The rest of the paper is organized as follows. In Sec. 2, we formulate basic equations for the considered hybrid NR-NE coupled system. In Sec. 3, we study dispersion characteristics and the field structure of the plasmonic modes in the NRs. In Sec. 4, we investigate the structure of the optical field of the laser emission in the system and the PP-mediated dynamics of the NEs coupled to NRs. In Section 5, we explore the phase transition exhibited by the total PP current in the lattice. Section 6 concludes the paper.

II. BASIC EQUATIONS

The system under the consideration is Fig. 1) contains a periodic 2D lattice of conducting NRs (NR) (7×7) with a randomly embedded rarefied set of quantum NEs (only four in Fig. 1, shown by solid circles) emitting the optical field. PPs are excited in the NRs and interact with the embedded NEs through the radiation field.

In Fig. 1 the NEs are connected by straight lines corresponding to the optimized path calculated using the TSP (traveling salesman problem) technique and Fermat's principle¹³. In such a configuration, the length of the connecting path A_D is proportional to the optimized (dimensionless) distance, which is a number of nodes in the numerical grid, which a photon can travel in the sample, passing each NE without visiting the same NE twice. Accordingly, A_D is calculated in the framework of our numerical analysis by dint of the TSP (traveling salesman problem) technique^{10,13}. The color scheme indicates that the embedded NEs in Fig. 1 consist of two clusters. To study this hybrid system, we use with time-dependent Maxwell's equations in the lattice of 2D NRs, coupled to the semi-classical rate equations for the electron populations in the NE¹¹.

The Maxwell equations are^{13,14}

$$\nabla \times \mathbf{E} = -\mu_0 \frac{\partial \mathbf{H}}{\partial t}, \quad \nabla \times \mathbf{H} = \varepsilon_0 \frac{\partial \mathbf{E}}{\partial t} + \mathbf{J} + \frac{\partial \mathbf{P}}{\partial t}, \quad (1)$$

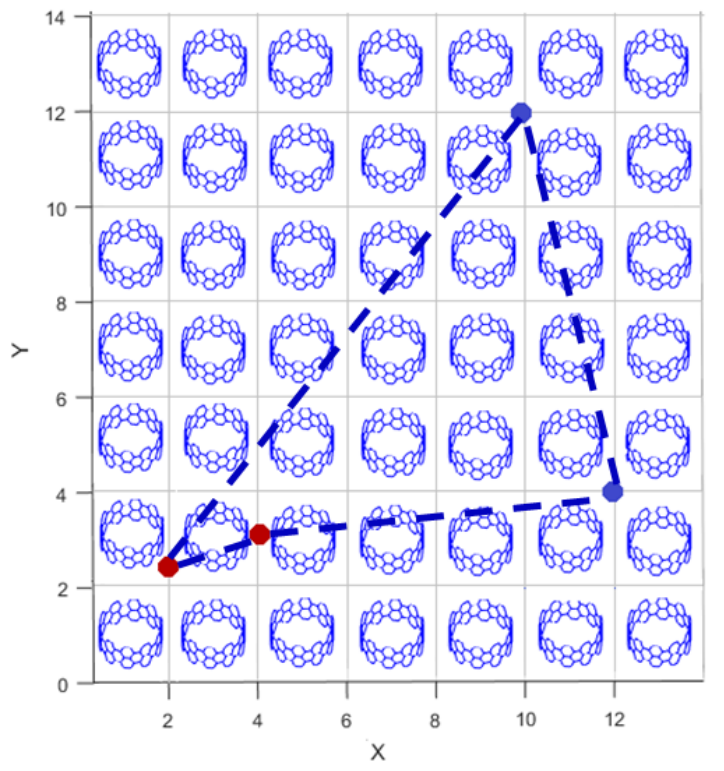


FIG. 1. The system is built as the lattice of size 7×7 . composed of conducting NRs with embedded quantum NEs (solid circles) emitting the optical field. In the present setup, four NEs form two clusters shown by red and blue colors. PPs are excited in the NRs and interact with the NEs. The NEs are connected by straight lines that correspond to the optimized path calculated by means of TSP (traveling salesman problem) method (with a traveling photon passing each NE without visiting the same NE twice) and Fermat's principle^{10,13}.

were $\mathbf{J} = \sum_k \mathbf{J}_k(\mathbf{R}_k^{\text{NR}}, t) \delta_{\mathbf{rR}_k^{\text{NR}}}$ is the PP electrical current in the NRs placed at spatial positions \mathbf{R}_k^{NR} , and $\mathbf{P} = \sum_k \mathbf{P}_k(\mathbf{R}_k^{\text{NE}}, t) \delta_{\mathbf{rR}_k^{\text{NE}}}$ is the electron polarization in the embedded NE placed at \mathbf{R}_k^{NE} . Here $\delta_{\mathbf{rR}}$ is the Kronecker's symbol, and the sums run over all NRs ($k = 1, N_r$) and NEs ($k = 1, N_s$). In Eq. (1) the electric current of the conducting electrons in the NRs obeys the material equation¹⁵ $\dot{\mathbf{J}}_k + \gamma_e \mathbf{J}_k = \varepsilon_0 \omega_p^2 \mathbf{E}$, where γ_e is the collision frequency of electrons, ω_p is the plasma frequency, as mentioned above, and ε_h is the dielectric constant of the host medium of NR. In the semi-classical approximation for non-interacting electrons, the evolution equation for \mathbf{P}_k in the vicinity of the embedded NE is¹¹

$$\frac{\partial^2 \mathbf{P}_k}{\partial t^2} + \Delta \omega_a \frac{\partial \mathbf{P}_k}{\partial t} + \omega_a^2 \mathbf{P}_k = \frac{6\pi \varepsilon_0 c^3}{\tau_{21} \omega_a^2} (N_{1,k} - N_{2,k}) \mathbf{E}_k. \quad (2)$$

To complete the model, we add the rate equations¹¹ for the occupation numbers of NEs, $N_{i,k} = N_i(\mathbf{R}_k^{\text{NE}}, t)$ (following¹⁴, we assume that the NEs are four-level quantum dots, as illustrated by Fig. 2):

$$\frac{\partial N_{0,k}}{\partial t} = -A_r N_{0,k} + \frac{N_{1,k}}{\tau_{13}}, \quad \frac{\partial N_{3,k}}{\partial t} = A_r N_{0,k} - \frac{N_{3,k}}{\tau_{02}}, \quad (3)$$

$$\frac{\partial N_{1,k}}{\partial t} = \frac{N_{2,k}}{\tau_{32}} - M_k - \frac{N_{1,k}}{\tau_{13}}, \quad \frac{\partial N_{2,k}}{\partial t} = \frac{N_{1,k}}{\tau_{12}} + M_k - \frac{N_{2,k}}{\tau_{02}}, \quad (4)$$

$$M_k = \frac{(\mathbf{I}_p \cdot \mathbf{E})_k}{\hbar \omega_a}, \quad \mathbf{I}_{p,k} = \frac{\partial \mathbf{P}_k}{\partial t}. \quad (5)$$

Here $\Delta\omega_a = \tau_{21}^{-1} + 2T_2^{-1}$, where T_2 is the mean time between dephasing events, τ_{21} is the decay time for the spontaneous transition from the second atomic level to the first one, ω_a is the radiation frequency (see e.g.¹¹), and M_k is the induced radiation rate or excitation rate, depending on its sign¹⁴. Note that components \mathbf{j}_{pk} parallel to \mathbf{E}_k mainly contribute to Eqs.(4) and (5)¹⁶. Coefficient A_r is the pump rate for the transition from the ground level (N_0) to the third one (N_3), which is proportional to the pump intensity in the experiment¹⁴.

The finite-difference time-domain (FDTD) numerical method¹⁷ was used to solve the model. In the simulations, we consider the gain medium with parameters of the GaN powder, see Refs.^{14,18}. In Eqs. (2) - (4), frequency ω_a is $2\pi \times 3 \times 10^{13}$ Hz, the lifetimes are $\tau_{32} = 0.3$ ps, $\tau_{10} = 1.6$ ps, $\tau_{21} = 16.6$ ps, and the dephasing time is $T_2 = 0.0218$ ps. In what follows we use the dimensionless time t normalized as $t \rightarrow tc/l_0$, where $l_0 = 100 \mu\text{m}$ is the typical spatial scale and c is the light velocity in vacuum. Thus, the present model couples the population-rate equations at different NE levels to the PP field equations in the vicinity of the NR lattice. Therefore, the NE resonant emission operation in the system is affected by the PP excitation in the NRs, which finally leads to essentially nonlinear field dynamics. Figure 3 shows the temporal dynamics of the PP field distribution in the 7×7 lattice of the conducting NRs (see Fig. 1), as produced by our FDTD simulations of Eqs. (1)-(5) at $\omega_p = 2.3$ THz at different simulation times t_f . In Fig. 3 the color-coding scheme for the field amplitude shows that, at short times < 40 , the PP field in the NR lattice is small. However, at longer times, an increasingly stronger PP field is generated in the lattice, gradually covering the entire lattice with time. The local field (designated by the red color) in the vicinity of NEs is large, as expected. Figure. 3 illustrates the temporal dynamics of the nonlinear transition forming the relationship between the NE oscillators and the PP in the underlying lattice. It shows why the chimera-like states under the study (recall they are

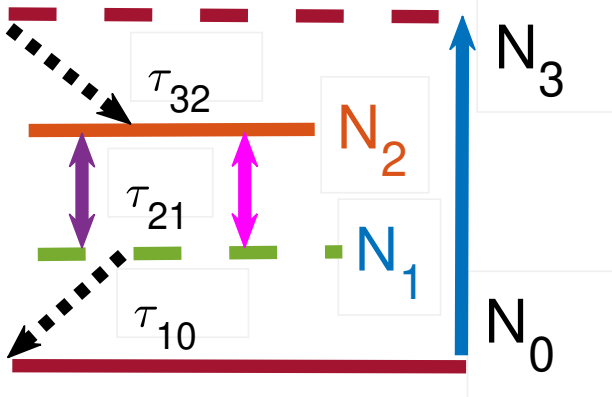


FIG. 2. The schematic representation of NE as a four-level system, see Eqs. (3)-(5). The external pump lifts electrons from the ground level (with population N_0) to the third level (with population N_3). After a short lifetime τ_{32} , the electrons perform the nonradiative transfer to the second level (with population N_2). The second level and the first level (with population N_1) are defined as the upper and lower lasing levels. Electrons are transferred from the upper level to the lower one by both spontaneous and stimulated emission. At last, electrons can perform the nonradiative transfer from the first level back to the ground one.

called chimeras as they combine the synchronized and desynchronized NE dynamical states) depend not only on time, but also on the plasma frequency ω_p of the surrounding NRs.

III. PLASMON MODES IN THE NRS (NANORINGS)

The transmission characteristics of surface PPs in ring resonators have been studied in nano-optics under the condition that the frequency dispersion may be neglected^{19,20}. However, this approximation is not applicable to the conducting NR in a vicinity of $\omega = \omega_p$. In the present section we briefly analyze the structure of the spectrum of a single nanoparticle. Below, the optical field in the NR lattice is studied by means of the FDTD technique, cf. Ref.¹⁷. As the most fundamental object, we consider a single cylindrical nanoparticle of radius R and length L_n , containing N_e valence electrons, assuming that the density of the valence electrons is uniform, $n(r) \equiv n_0$. The cylindrical geometry admits the propagation of independent TM ($[E_{\parallel}, H_{\perp}]$) and TE ($[E_{\perp}, H_{\parallel}]$) modes with the longitudinal and transverse components of the electric field, the corresponding subscripts being denoted below as $\alpha = \parallel$ and $\alpha = \perp$ components, respectively. Following¹⁶, we define shift \mathbf{u}_{α} of the

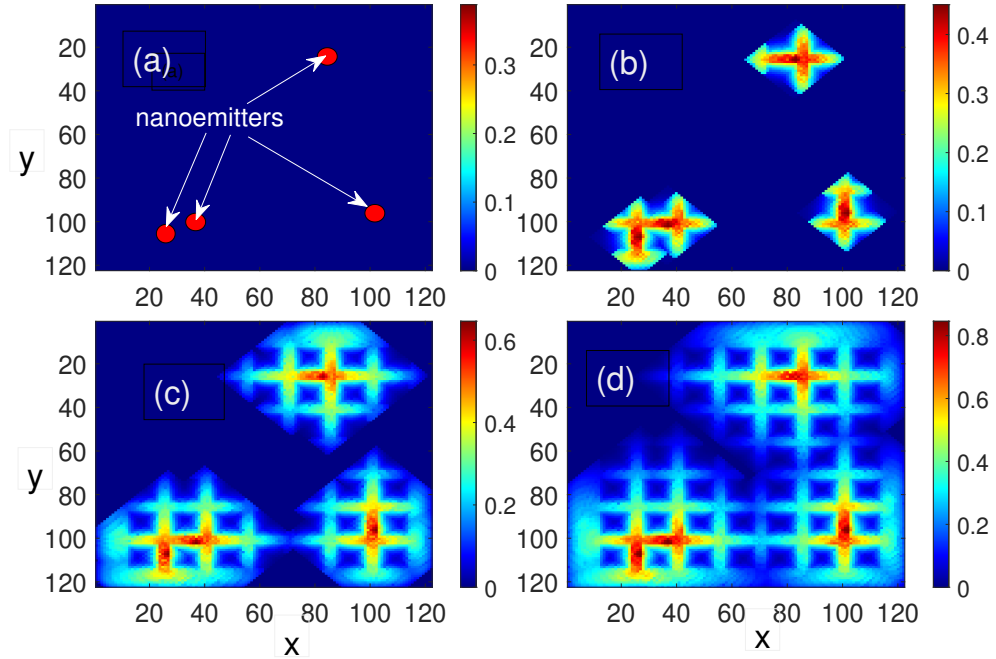


FIG. 3. The temporal dynamics (FDTD) of spatial distribution of the PP field generated by NEs in the 7×7 lattice of conducting NRs (see Fig. 1) at $\omega_p = 2.3$ THz at different simulating times t_f : (a) 20, (b) 40, (c) 60, (d) 80. The color coding represents values of the field amplitude.) At long times $t_f > 60$, the PP field, generated in the NR lattice by NEs, gradually covers nearly the entire NR lattice. The local field (shown by the red color) in the vicinity of NEs (see panel (a)) is the largest. The optical field is concentrated in gaps of the NR lattice and practically does not penetrate into the NRs.

electron distribution, hence one can calculate the respective displaced density as $n(\mathbf{r} - \mathbf{u}_\alpha) \approx n(\mathbf{r}) + \delta n_\alpha$. For small u_α , one has

$$\delta n_\alpha(\mathbf{r}) = -\mathbf{u}_\alpha \cdot \nabla n(\mathbf{r}). \quad (6)$$

The corresponding energy variation is

$$\delta E_\alpha = \frac{e^2}{2} \int d^3\mathbf{r} \int d^3\mathbf{r}' \frac{\delta n_\alpha(\mathbf{r}) \delta n_\alpha(\mathbf{r}')}{|\mathbf{r} - \mathbf{r}'|}, \quad (7)$$

therefore the restoring force is $F_\alpha = -\frac{\partial}{\partial u_\alpha} (\delta E_\alpha) = -k_\alpha u_\alpha$, hence the normal-mode's frequency is

$$\omega_{0,\alpha} = \sqrt{\frac{k_\alpha}{M_e}}. \quad (8)$$

Here $M_e = N_e m_e$ is the full mass of the electrons, while k_α is the effective spring constant.

For the longitudinal displacement $\mathbf{u}_{\alpha=\parallel}$, the variation of the energy in Eq. (7) can be written as

$$\delta E_{\parallel} = 2\pi^2 (eun_0)^2 R^3 x [1 - 2y(x)], \quad x = L_n/R, \quad (9)$$

where $y(x) = (g(x) - 4/3)/(\pi x)$, and

$$g(x) = \frac{x}{6} \left[(x^2 + 4) K\left(-\frac{4}{x^2}\right) - (x^2 - 4) E\left(-\frac{4}{x^2}\right) \right], \quad (10)$$

with the complete elliptic integrals of the first and second kinds, respectively.

$$K(x) = \int_0^1 \frac{dt}{\sqrt{(1-t^2)(1-xt^2)}}, \quad E(x) = \int_0^1 dt \sqrt{\frac{1-xt^2}{1-t^2}}. \quad (11)$$

In this case the normal-frequency mode can be expressed as

$$\omega_{0,\parallel} = \omega_p \sqrt{1 - 2y(x)}, \quad (12)$$

where $\omega_p = (n_0 e^2 / \varepsilon_0 m_e)^{1/2}$, and the electron density is $n_0 = N_e / \pi R^2 L_n$. In the thin-disk limit ($x = L_n/R \ll 1$) we obtain¹⁶

$$\omega_{0,\parallel}^{\text{disk}} \simeq \omega_p \left\{ 1 - \frac{L_n}{4\pi R} \left[6 \ln 2 - 1 - 2 \ln \left(\frac{L_n}{R} \right) \right] \right\}, \quad L_n/R \ll 1, \quad (13)$$

which approaches the ω_p in the limit of ($L_n/R \rightarrow 0$), see details in Fig. 4.

The case of the transverse plasmonic mode of the TE type ($\alpha = \perp$) can be studied in a similar way as done above for the longitudinal mode, which results in the following expression for the transverse mode frequency

$$\omega_{0,\perp} = \omega_p \sqrt{y(x)}, \quad x \equiv L_n/R. \quad (14)$$

In Fig. 4 the solid lines show dependencies of $\omega_{\parallel}/\omega_p$ and ω_{\perp}/ω_p on $x = L_n/R$ in the interval $[0, 3]$, while the dotted lines show the corresponding approximate solutions. It is seen that the latter approximations are valid for $L_n/R < 0.9$. Besides, it is seen Fig. 4 that the contribution of E_{\perp} is small at $|x| \ll 1$, hence the contribution of E_{\perp} becomes comparable with E_{\parallel} at $x \sim 2$, which corresponds to a cylindrical particle, rather than the ring studied here.

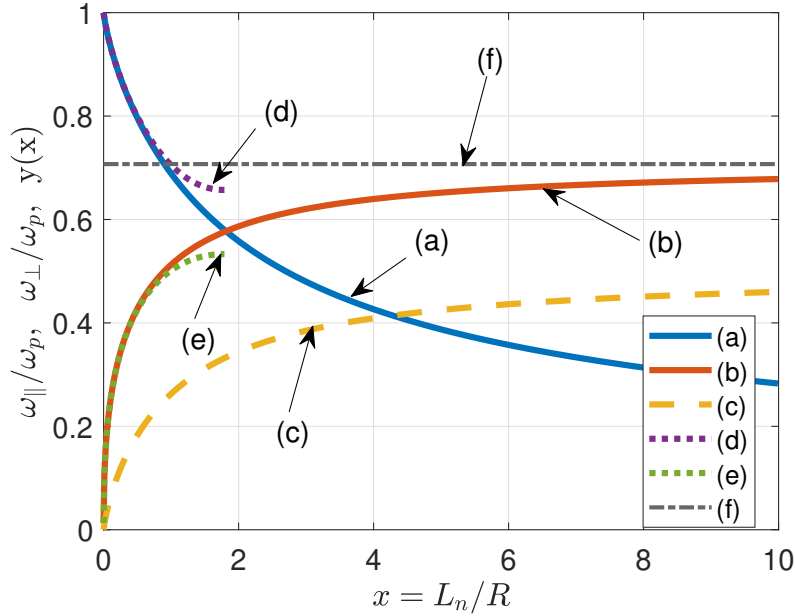


FIG. 4. Dependencies $\omega_{\parallel}/\omega_p$ (a) and ω_{\perp}/ω_p (b) on parameter $x = L_n/R$ in the interval $[0, 10]$, see Eqs.(13) and (14) respectively. Dotted lines ((d) and (e)) show the approximate solutions. It is seen that such an approximation is correct only for $L_n/R < 0.9$. At $x \approx 1.75$ the values of ω_{\parallel} and ω_{\perp} are close. The yellow dashed line (c) displays the function $y(x)$ from Eq.(9), and the black line (f) displays the asymptotic value $1/\sqrt{2}$ of the normalized surface plasmon frequency for $x \gg 1$.

IV. RESONANT EMISSION OF NANOEMITTERS IN THE SYSTEM WITH NRS

In this section, we study the dynamics of the system of Eqs. (1)-(4), which combines the Maxwell's equations for the PP field with the semiclassical approximation for the optical field emission from the NEs. We apply the FDTD technique to calculate the field in the NR lattice with the incorporated NEs. Our system (see Fig. (1)) contains the periodic lattice of conducting NRs (of the size 7×7) with embedded NEs emitting the optical field. PPs are excited in the NRs and interact with the NEs. In Fig. (1), the NEs are connected by dashed blue lines that correspond to the TSP optimized path (when, as said above, a traveling photon passes each NE, without visiting the same NE twice¹⁰). We use an advanced technique where the standard FDTD approach is extended by calculating the dynamics of the semiclassical polarization system (see Eq. (2)) coupled to the population dynamics in the four-level laser NEs (Eqs. (3)-(4)), at each time step, see further details in

Ref.²¹. In this work, numerical calculations were performed by means of the standard FDTD technique¹⁵. Also, the open source package **fdtd** was used, which allowed us to include the necessary extensions related to the modeling of the Drude frequency dispersion in NRs, see link [<https://github.com/flaport/fdtd>] for further details. To simulate the field dynamics in the hybrid system with open boundaries the standard perfectly matched layer (PML) boundary conditions are applied at boundaries of the FDTD grid, to avoid the reflection of electromagnetic waves from the boundary¹⁵. On the adopted scale, the typical NE size is orders of magnitude smaller than the typical NR size, therefore the NEs are approximated here by the point-like sources. In our simulations we dealt with the general 3D vector electromagnetic fields **E** and **H** in the general form. The simulations demonstrate that, in the present system, TM electromagnetic waves with components $[E_z, H_x, H_y]$ are mainly generated. This conclusion agrees with the theory Ref.¹⁶, where it was shown that, in the case of nano-objects in the disk limit ($L_n/R \ll 1$, where R and L_n are the radius and height, respectively) the main contribution yields the E_z (alias E_{\parallel}) longitudinal field, while the transverse field is conspicuous at $L_n/R \sim 1$ ¹⁶. Thus, in the disk limit one can obtain $\omega_{0,\parallel} \simeq \omega_p$, which approaches the ω_p value in the considered limit of $L_n/R \rightarrow 0$. For the TE mode, the transverse frequency is estimated as $\omega_{0,\perp}/\omega_p \sim \sqrt{L_n/R}$, which is small in the present case, $L_n/R \rightarrow 0$. To make the following figures clear, only the $|E_z|$ field components are displayed in them. The dynamics of the present hybrid system significantly depends on frequency ω_p of the dispersive NRs in the terahertz range. Therefore, in the following we focus on two cases. *viz.*, $\omega_p = 2.3$ THz and $\omega_p = 2.3 \times 10^{-2}$ THz, in which ω_p differs by two order of magnitude.

Figure 5 displays the dynamics produced by the numerical solution of Eqs.(1)-(5) for the 7×7 NR lattice for two different NE plasma frequencies, $\omega_p = 2.3 \times 10^{-2}$ and 2.3 THz. Panels (a) and (b) display the dynamics of the populations of the resonant emission NE levels $N_{1,2}$, see Eq.(4) (the evolution of $N_{0,3}$ is not displayed here). Panels (c) and (d) show the evolution of the average quantum polarization $|\mathbf{P}|$ and photocurrent $i_{ph} = \partial|\mathbf{P}|/\partial t$. Further, panels (e) and (f) show details of the average NR current $\langle J \rangle$, see Eq.(15). We observe that in both cases the evolution of $\langle J \rangle$ drastically differs for different values of ω_p . At $\omega_p = 2.3$ THz, the amplitude of $\langle J \rangle$ is significantly larger than at $\omega_p = 0.023$ THz. It is seen that, at large times $t > 60$, the evolution is chaotic, weakly depending on details of the NE distribution. Such a behavior of $N_{1,2}$, displayed in Fig. 5, indicates the onset of the

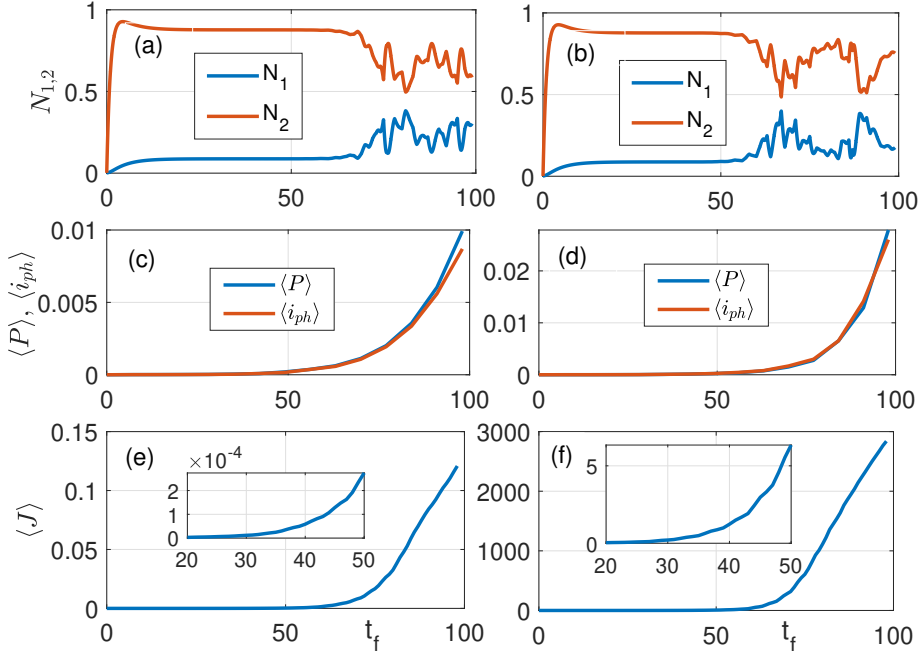


FIG. 5. The temporal dynamics produced by the numerical solution of the system of Eq.(1)-(5) for the 7×7 NR lattice with two different plasma frequencies: $\omega_p = 2.3 \times 10^{-2}$ THz (the left) and 2.3 THz (the left and right columns, respectively). Here (a) and (b) show the dynamics of populations N_1 and N_2 of the NE lasing levels, respectively (see Eq. (4); the dynamics of populations $N_{0,3}$, see Eq. (3), is not displayed here). (c,d) The average quantum polarization $|\mathbf{P}|$ and photocurrent $i_{ph} = \partial|\mathbf{P}|/\partial t$. Panels (e) and (f) exhibit a drastic difference in the average current $\langle J \rangle$ (see Eq. (15)) in NRs at $\omega_p < \omega_c$ (the left) and $\omega_p > \omega_c$ ((e) and (f), respectively).

effective coupling of the PP and NE subsystems, which significantly depends on ω_p .

Fig. 6 exhibits details of the population dynamics for $N_{0,1,2,3}$ of the 4-level NE at $t_f > 20$, when the system commences the transit to the nonlinear regime. Red and yellow lines represent, respectively, populations N_1 and N_2 of the lasing levels, while the green and purple lines correspond to N_0 and N_3 , respectively. The light blue line shows the conservation of $N = N_0 + N_1 + N_2 + N_3$. From Fig. 6, it can be seen that, at $t_f > 58$, the stationary values of the population levels become unstable and convert into a nonlinear oscillatory regime. To define the time when the instability commences, we studied the behavior of the Lyapunov function E_L . The blue line in Fig. 6 instability) at $t_f > 60$. Further analysis shows that such an instability is regularized by the transition to a regime of nonlinear oscillations between the laser levels N_1 and N_2 . To get more insight into the dynamics in the hybrid system, it

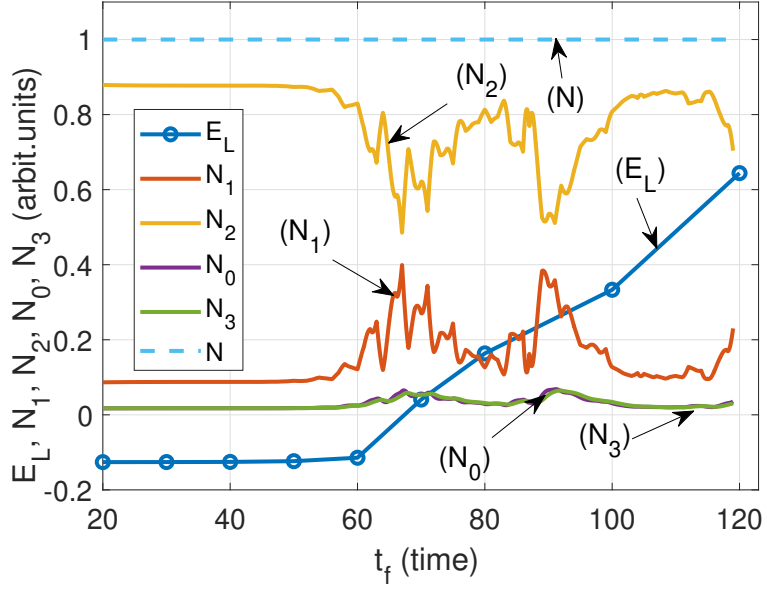


FIG. 6. The dynamics of populations $N_{0,1,2,3}$ of the 4-level NE. Red and yellow lines represent, respectively, populations N_1 and N_2 of the lasing levels. The light blue line shows the conservation of $N = N_0 + N_1 + N_2 + N_3$. The blue line exhibits the largest Lyapunov exponent, which changes its value from negative to positive (switching to instability) at dimensionless calculation time $t_f > 60$.

is instructive to consider the average current $\langle J \rangle$ in the NR conductive lattice, which is

$$\langle J \rangle = \langle J(\omega_p) \rangle_{N_r} = (N_r)^{-2} \sqrt{\sum |J_{i,j}|^2}, \quad (15)$$

where $J_{i,j}$ is the current in the NR with coordinates (i, j) , and the summation is performed over the entire NR lattice, N_r being the total number of NRs. Figure 7(a) shows the average PP current $\langle J \rangle$ in the conducting lattice of 7×7 of NRs, see Eq. (15), as a function of the scaled simulation time t_f and plasma frequency ω_p . It is seen that $\langle J \rangle$ emerges from zero at $t_f \approx 55$ and sharply increases at $\omega_p \geq \omega_c \simeq 0.5$ THz, which is a critical value of ω_p indicating the appearance of the strong coupling between the PP current in the NR lattice and the emission field in the embedded quantum NEs. The critical value ω_c can be extracted from the data with the help of the standard fitting technique. Figure. 7(b) exhibits the fitting of $\langle J \rangle$ by function

$$\left\langle J \left(\frac{\omega_p}{\omega_c} \right) \right\rangle \propto F(x) = a \cdot [\text{erf}(\log(x/b)) + 1], \text{ where } \text{erf}(z) = \frac{2}{\sqrt{\pi}} \int_0^z e^{-z^2} dz. \quad (16)$$

Using the data from our FDTD simulations for $\langle J \rangle$ and Eq. (16) allowed us to extract both fitting parameters $a = 0.495$ and $b = 25$ that correspond to $\omega_c = 4.927 \times 10^{11}$ Hz [see the

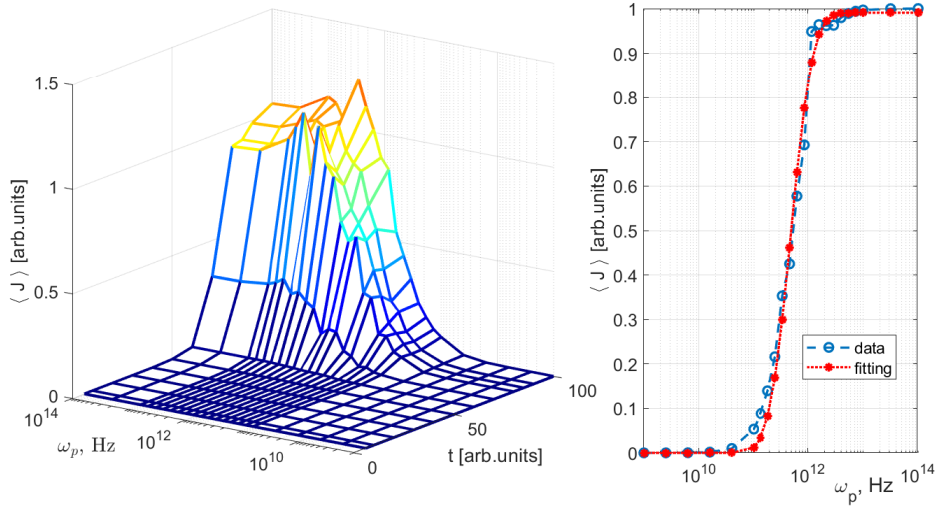


FIG. 7. (a) The average PP current $\langle J \rangle$ in the conducting lattice of 7×7 NRs as a function time t_f and the NR plasma frequency ω_p . It is seen that $\langle J \rangle$ emerges from zero at $t_f \approx 55$ for $\omega_p \geq \omega_c \simeq 3 \times 10^{11}$ Hz; (b) the normalized value $\langle J(\omega_p) \rangle$ and its fitting by the $\text{err}(\omega_p)$ function, which is found from the FDTD data, see details in the text.

blue and red lines in Fig. 7(b), respectively] within 95% confidence bounds. The numerical package NumPy 2.2.0 (see <https://numpy.org>) was used for this purpose.

To explore details of the nonlinear internal dynamics of the radiating NEs, we calculated the correlation functions (CF) of the z -component of the photocurrent,

$$I_{ij}(t_f, \omega_p) = [\mathbf{I}_p \Theta(t_f)]_z, \parallel z\text{-axis of NRs} \quad (17)$$

for different NE pairs (i, j) (see Fig. 1) for various values of t_f , where $\Theta(x)$ is the Heaviside step function. The cross-correlation function $\text{CF}(I_i I_j)$ as a function of the time lag $\tau^{22,23}$ is (n is NE number)

$$\text{CF}_{ij}(t_f, \omega_p | \tau) = \text{CF}(I_i I_j) = \frac{1}{n s_i s_j} \sum_{m=1}^n \Delta I_i(t_m) \Delta I_j(t_m + \tau), \quad (18)$$

where $\Delta I_i(t_m) = I_i(t_m) - \bar{I}_i$, \bar{I}_i is the mean value, and $s_k^2 = 1/(n-1) \sum_{m=1}^n \Delta I_k(t_m)^2$.

Figure 8 displays the cross-correlation function of the photocurrents CF_{12} (see Eq.(18)) for different times t_f at fixed $\omega_p = 2.3$ THz for the FDTD solutions of the system of Eqs. (1)-(5). From Fig. 8 it is seen that, at small $t_f \leq 40$, CF_{12} rapidly decays, but at $t_f \geq 60$ the correlations significantly increase, due to the establishment of collective synchronization between all the NEs through the laser emission.

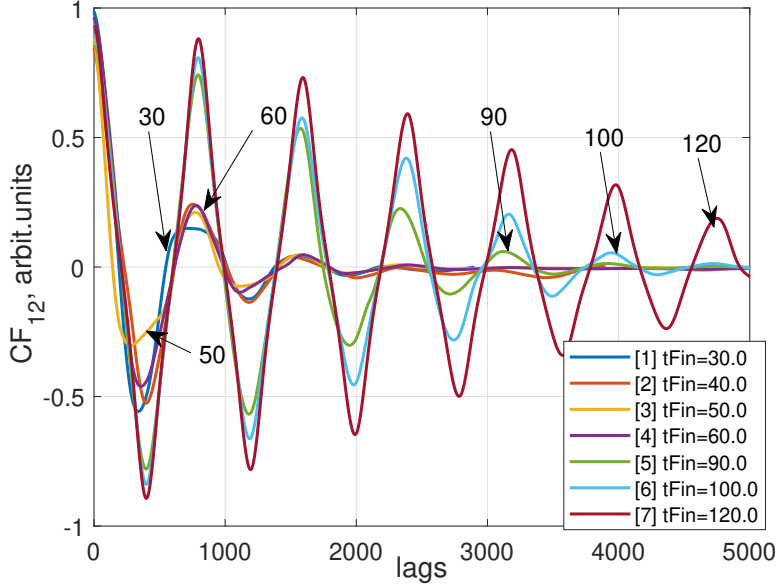


FIG. 8. The cross-correlation function of the photocurrent CF_{12} for the NEs with numbers 1 and 2 at different times t_f and $\omega_p = 2.3$ THz, produced by the FDTD solutions of the system of Eqs.(1)-(5). It is seen that, at small times, $t_f \leq 40$, CF_{12} rapidly decays, but at larger times, $t_f \geq 60$, the level of the NE cross-correlations in the lattice significantly increases.

It is interesting to study the dependence of the correlation on the NR plasma frequency ω_p . Such a study turns out to be more instructive when comparing the residuals of the cross-correlation functions of the NE photocurrents,

$$\widehat{R}(t_f, \omega_p) = R_{ij,km}(t_f, \omega_p) = \sum_l [CF_{ij}(t_f, \omega_p | \tau_l) - CF_{km}(t_f, \omega_p | \tau_l)]^2, \quad (19)$$

as a function of ω_p . Figure 9 shows a family of such dependencies $R(\omega_p)$ for different times t_f and different NE pairs (i, j) and (k, m) .

In Fig. 9, the black dashed lines indicate the transition region in terms of the average current $\langle J \rangle$, see Eq.(15). Figure 9 demonstrates the appearance, in the transition region, of a zone similar to chimera states (shown by isolated circles). In this range, even a small variation of ω_p leads to a significant change in the magnitude of the cross-correlations of the NE pairs. This fact indicates that, for the coupled PPs and NEs, the dynamics of the optical field in the quantum NE subsystem essentially depends on ω_p , which is a parameter of the classical NR subsystem. Further, the black dashed lines allow one to compare the classical PP dynamics in the NRs with the dynamics of the quantum NE subsystem (photocurrent)

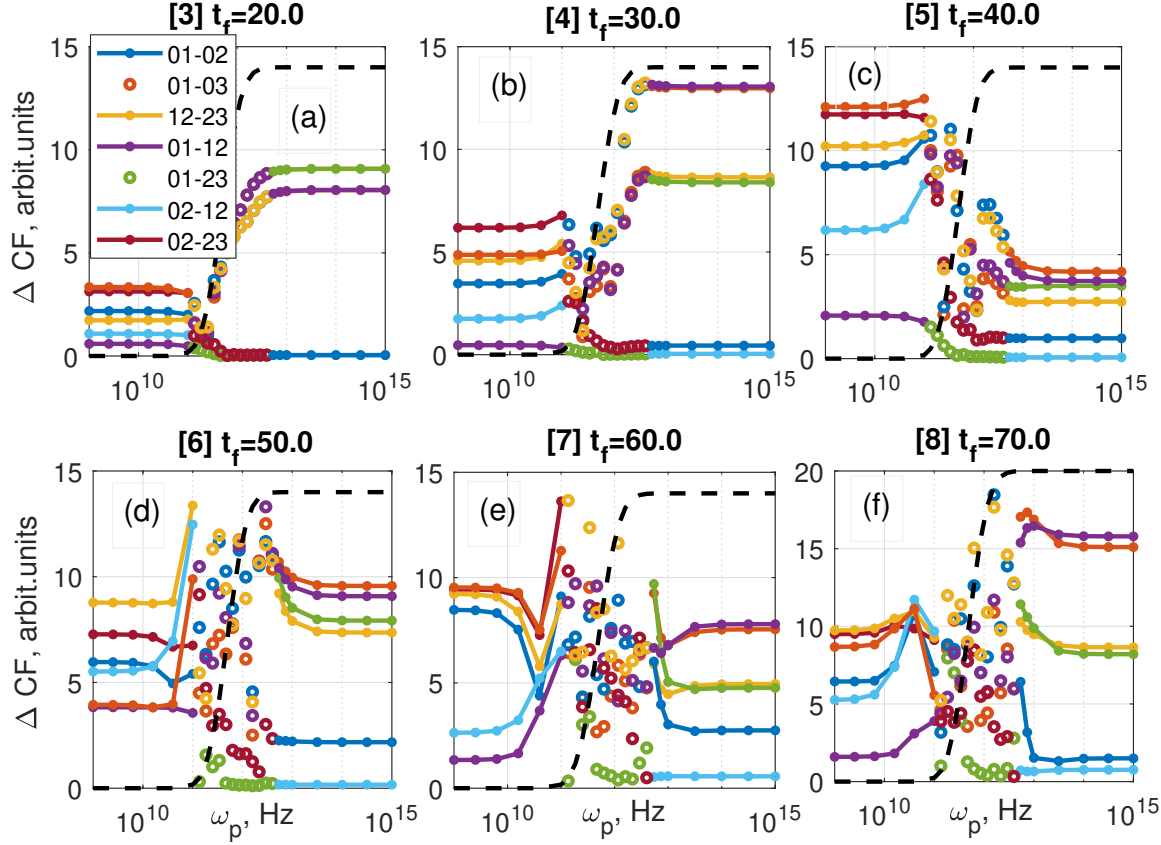


FIG. 9. The $\hat{R}(t_f, \omega_p)$ norm (see Eq.(19)) of the residual of the cross-correlations of the photocurrents for different NE pairs (i, j) and (k, m) (see the legend in panel (a)) as a function of ω_p , for different t_f : (a) 20, (b) 30, (c) 40, (d) 50, (e) 60, (f) 70. The color lines correspond to $(i, j) - (k, l)$ NE pairs. The black line indicates the transition region [see Fig. (7)(b)] of average current $\langle J \rangle$ in the NR lattice [see Eq. (15)]. We observe the chimera-like states (isolated points) in the transition area.

in the critical region, $100 \text{ GHz} < \omega_p < 1 \text{ THz}$. From Fig. 9 it is seen that, outside the critical region the branches of the $\hat{R}(t_f, \omega_p)$ curves are smooth, which makes it possible to connect them by solid lines (as a guide for the eye). This fact implies a weak coupling between the PP and NE subsystems in this range, where the conducting NR is actually a dielectric (roughly, at $\omega_p \lesssim 10 \text{ GHz}$). Note also that, as seen from Fig. 9, in this configuration $\hat{R}(\omega_p)$ remains small for the NE pairs $(0, 1) - (0, 2)$ and $(0, 2) - (1, 2)$, therefore those pairs are insignificant. This, it is seen in Fig. 9(a) that, at $t_f = 20$, the curve $\hat{R}(\omega_p)$ has a characteristic smooth shape, the details of which depend on t_f . At $t_f = 20$, as ω_p is approaching the critical value ω_c from below, the $\hat{R}(t_f, \omega_p)$ remains a smooth function of ω_p with a local minimum.

At $t_f = 30$, see panel (b), this minimum deepens, and the dependence $\hat{R}(t_f, \omega_p)$ loses its smoothness in the critical region. In this zone, due to their chaotic positions, the connection of adjacent points loses its meaning, and in Fig. 9 they appear as a cloud of isolated points. Our calculations show that, in the critical region, the standard deviation²⁴ of the value of $\hat{R}(t_f, \omega_p)$ is significantly higher than outside of it. As can be seen from Figs. 9(c-f), with the further increase of τ_f towards $t_f > 50$, the apparently chaotic set of points in the critical region cease changing. Outside the critical region the dependencies $\hat{R}(\omega_p)$ are smooth.

V. DISCUSSION

We have addressed the coupling of the NEs (nanoemitters) and PPs (plasma polaritons) in the hybrid system, built as the periodic lattice of conducting NRs (nanorings) with embedded NEs, through the common optical field. The structure of the field significantly depends on the NR plasma frequency ω_p . At the critical value of ω_p , the phase transition occurs in the system, leading to the sharp increase in the average NR current. In this case, the PP field disturbs the internal degrees of freedom of the quantum NEs, inducing the cross-correlation of the photocurrents in all NEs, the correlation magnitude significantly depending on ω_p . The instability of the NE resonant emission leads to the appearance of non-smooth (chimera- or chaos-like) features. In this regime, a small variation in ω_p leads to a significant change in the magnitude of the cross-correlations of NE pairs. Figure 9 exhibits a possibility of the coexistence of the localized synchronized and desynchronized cross-correlations of NEs embedded in the lattice of identical NRs, which results in the formatting of inhomogeneous states in the hybrid system. Similar (quasi-chaotic) behavior is well known in Kuramoto systems of coupled oscillators^{25,26}. Patterns featuring this behavior are unstable and are identified as chimeras²⁷. It is instructive to study the evolution of such irregular states. Figure 3 shows a typical size of the field regions surrounding PPs in the NR lattice. Initially these areas are well separated and expand with the increase of time t_f up to $t_f \sim 80$, when the expanding areas overlap. The latter means that initially desynchronized (due to the spontaneous emission) NEs develop the synchronization (induced emission) at $t_f \sim 80$. Following the commonly adopted (scalar) metric S of a curve for the non-smoothness²⁸, we define the non-smoothness S for our case (the instability of cross-correlations of NE pairs)

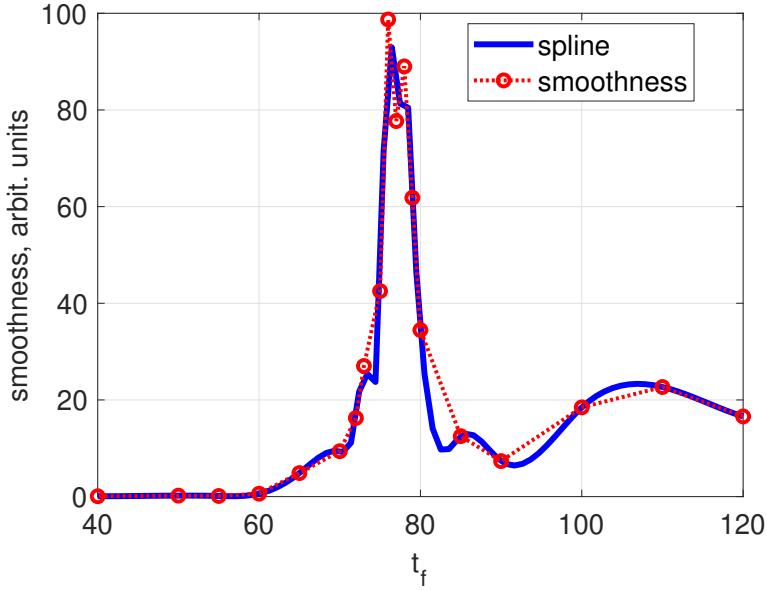


FIG. 10. The maximum value of the non-smoothness parameter, $S(t_f)_{\max} = \max(S_{t_f})$ of the chimera-like states (red points), displayed in panels (a-e) of Fig. 9, for all the NE pairs, as a function of time t_f in the area of $\omega \sim \omega_c$ (see Fig. 9). S_{\max} attains the largest value at $t_f \approx 76$, indicating a highly non-smooth structure, as expected for chimera states^{12,25}.

as

$$S(t_f) = \int \left(\frac{d^2 f(t_f, \omega)}{d\omega^2} \right)^2 d\omega, \quad f(t_f, \omega_p) = \hat{R}(t_f, \omega_p) \quad (20)$$

over the curve's domain ω_p (with \hat{R} defined by Eq. (19)), see panels (a-f) in Fig. 9. A lower value of $S(t_f)$ evidently indicates a smoother curve. (The natural cubic spline minimizes the L_2 norm of the second derivative among all C_2 the function continuous with its first and second derivatives, interpolating functions passing through the given points²⁸.) In the present system, the critical behavior occurs in nonlinear quantum NEs in the respective range of values of the plasma frequency ω_p in the NR lattice.

As Fig. 6 shows, the maximum Lyapunov exponent takes positive values in the critical region, indicating unstable dynamics of the system. Figure 3 demonstrates, as said above, that the effective coupling of the NE oscillators to the PPs in the periodic NR lattice leads to the dependence of the evolution of the corresponding chimera-like states on the NR parameter ω_p . Ref.²⁹ reported an advanced technology based on hybrid nanomaterials, such as sandwiched graphene oxide, and self-assembly of carbon nanotubes (CNT) into CNT

rings. The latter, in particular, allows adjusting ω_p of CNT rings to the desired range of ω_p .

VI. CONCLUSION

We have studied the hybrid system, built as the NR lattice carrying PPs with the non-linear quantum NEs embedded in the lattice. It is found that the strong coupling between the PPs and NEs, mediated by the optical field, leads to the significant cross-correlation between NE pairs, so that the NE dynamics demonstrates essential dependence on the NR plasma frequency ω_p . However, at larger $\omega_p \geq \omega_c$ a transition occurs to the state in which the PP field produces a significant contribution to the radiation field, which perturbs the dynamics of NEs, leading to a change in their cross-correlations. In such a system, the NEs are coupled to the PP field in the NRs, which contributes to the NEs' optical field. As ω_p increases, the PP field attains a significant amplitude, which causes a strong coupling between PPs and NEs and reorientation of the field direction parallel to the PP field in the NRs. This fact leads to a significant dependence of the shape of the cross-correlation of photocurrents in NE pairs on the plasma frequency ω_p of the NRs coupled to the NEs.

VII. ACKNOWLEDGMENT

G. M.-A. acknowledges a fellowship provided by the CONAHCYT-México.

VIII. DISCLOSURES

The authors declare no conflicts of interest.

IX. DATA AVAILABILITY STATEMENT

The data that support the main findings of this study are available in a publicly accessible repository at the link <https://drive.google.com/drive/folders/1w-uolJk15X0rIBNLozCk850TC-BbxB?usp=sharing> and from the corresponding author upon reasonable request.

REFERENCES

¹Kun Ba and Jianlu Wang. Advances in solution-processed quantum dots based hybrid structures for infrared photodetector. *Materials Today*, 58:119–134, 2022.

²A.G.U. Perera. Chapter 5 - homo- and heterojunction interfacial workfunction internal photo-emission detectors from uv to ir. In Sarath D. Gunapala, David R. Rhiger, and Chennupati Jagadish, editors, *Advances in Infrared Photodetectors*, volume 84 of *Semiconductors and Semimetals*, pages 243–302. Elsevier, 2011.

³Ravinder K. Jain, Anthony J. Hoffman, Peter Uhd Jepsen, Peter Q Liu, Dmitry Turchinovich, and Miriam Serena Vitiello. Mid-infrared, long-wave infrared, and terahertz photonics: introduction. *Opt. Express*, 28(9):14169–14175, Apr 2020.

⁴Tongyu Dai, Shuangxing Guo, Xiaoming Duan, Renqin Dou, and Qingli Zhang. High efficiency single-longitudinal-mode resonantly-pumped ho:gtdao4 laser at 2068nm. *Opt. Express*, 27(23):34204–34210, Nov 2019.

⁵Victor Ryzhii, Maxim Ryzhii, Vladimir Mitin, Michael S. Shur, and Taiichi Otsuji. Far-infrared photodetectors based on graphene/black-asp heterostructures. *Opt. Express*, 28(2):2480–2498, Jan 2020.

⁶I. Arrazola, R. Hillenbrand, and A. Yu. Nikitin. Plasmons in graphene on uniaxial substrates. *Applied Physics Letters*, 104(1):011111, 01 2014.

⁷J. Guo, K. Black, J. Hu, and M. Singh. Study of plasmonics in hybrids made from a quantum emitter and double metallic nanoshell dimer. *J. Phys. Condens. Matter.*, 30:, 185301, 2018.

⁸Severin N. Habisreutinger and Jeffrey L. Blackburn. Carbon nanotubes in high-performance perovskite photovoltaics and other emerging optoelectronic applications. *Journal of Applied Physics*, 129(1):010903, 01 2021.

⁹Gennadiy Burlak, Gustavo Medina-Angel, and Yessica Calderon-Segura. Plasmon-mediated dynamics and lasing of nanoemitters enhanced by dispersing nanorings. *The Journal of Chemical Physics*, 161(3):034110, 07 2024.

¹⁰Gennadiy Burlak, A. Díaz de Anda, Boris A. Malomed, E. Martínez-Sánchez, G. Medina-Ángel, R. Morales-Nava, J.J. Martínez-Ocampo, M.E. de Anda-Reyes, and A. Romero-López. Critical properties of the optical field localization in a three-dimensional percolating system: Theory and experiment. *Chaos, Solitons & Fractals*, 173:113734, 2023.

¹¹A. E. Siegman. *Lasers*. Mill Valley, California, 1986.

¹²Daniel M. Abrams and Steven H. Strogatz. Chimera states for coupled oscillators. *Phys. Rev. Lett.*, 93:174102, Oct 2004.

¹³Gennadiy Burlak and Y. G. Rubo. Mirrorless lasing from light emitters in percolating clusters. *Phys. Rev. A*, 92:013812, Jul 2015.

¹⁴Xunya Jiang and C. M. Soukoulis. Time dependent theory for random lasers. *Phys. Rev. Lett.*, 85:70–73, Jul 2000.

¹⁵A. Taflove and S.C. Hagness. *Computational Electrodynamics: The Finite-Difference Time-Domain Methods*. Artech House (Boston), 2005.

¹⁶Charles A. Downing and Guillaume Weick. Plasmonic modes in cylindrical nanoparticles and dimers. *Proceedings of the Royal Society A: Mathematical, Physical and Engineering Sciences*, 476(2244):20200530, 2020.

¹⁷A. Taflove and S. C. Hagness. *Computational Electrodynamics: The Finite-Difference Time-Domain Method, 3rd ed.* Artech House, Norwood, MA, 2005.

¹⁸H. Cao, Y. G. Zhao, S. T. Ho, E. W. Seelig, Q. H. Wang, and R. P. H. Chang. Random laser action in semiconductor powder. *Phys. Rev. Lett.*, 82:2278–2281, Mar 1999.

¹⁹Tong-Biao Wang, Xie-Wen Wen, Cheng-Ping Yin, and He-Zhou Wang. The transmission characteristics of surface plasmon polaritons in ring resonator. *Opt. Express*, 17(26):24096–24101, Dec 2009.

²⁰I. Wolff and N. Knoppik. Microstrip ring resonator and dispersion measurement on microstrip lines. *Electronics Letters*, 7(26):779–781, 1971.

²¹Gennadiy Burlak and Gustavo Medina-Ángel. Extended dynamics and lasing of nanoemitters enhanced by dispersing single-walled carbon nanotubes. *Journal of Quantitative Spectroscopy and Radiative Transfer*, 296:108463, 2023.

²²Charles Therrien and Murali Tummala. *Probability and random processes for electrical and computer engineers*. CRC press, 2018.

²³Caitlin R. S. Williams, Thomas E. Murphy, Rajarshi Roy, Francesco Sorrentino, Thomas Dahms, and Eckehard Schöll. Experimental observations of group synchrony in a system of chaotic optoelectronic oscillators. *Phys. Rev. Lett.*, 110:064104, Feb 2013.

²⁴John A. Gubner. *Probability and random processes for electrical and computer engineers*. Cambridge University Press & Assessment, 2006.

²⁵Jörn Davidsen, Yuri Maistrenko, and Kenneth Showalter. Introduction to focus issue: Chimera states: From theory and experiments to technology and living systems. *Chaos: An Interdisciplinary Journal of Nonlinear Science*, 34(12):120402, 12 2024.

²⁶Hon Wai Hana Lau, Jörn Davidsen, and Christoph Simon. Chimera patterns in conservative hamiltonian systems and bose-einstein condensates of ultracold atoms. *Scientific Reports*, 13(1):8590, 2023.

²⁷Felix P. Kemeth, Sindre W. Haugland, Lennart Schmidt, Ioannis G. Kevrekidis, and Katharina Krischer. A classification scheme for chimera states. *Chaos: An Interdisciplinary Journal of Nonlinear Science*, 26(9):094815, 08 2016.

²⁸William H Press, Saul A Teukolsky, William T Vetterling, and Brian P Flannery. *Numerical recipes example book (c++): The art of scientific computing*. Cambridge University Press, Cambridge, 2002.

²⁹J. Song, F. Wang, X. Yang, B. Ning, M.G. Harp, S.H. Culp, S. Hu, P. Huang, L. Nie, and J. Chen. Gold nanoparticle coated carbon nanotube ring with enhanced raman scattering and photothermal conversion property for theranostic applications. *Journal of the American Chemical Society*, 138:7005–7015, 2016.